Airfoil Dynamic Stall at Constant Pitch Rate and High Reynolds Number

Peter F. Lorber* and Franklin O. Carta†
United Technologies Research Center, East Hartford, Connecticut

An experiment has been performed to study the aerodynamics of dynamic stall penetration at constant pitch rate and high Reynolds number, in an attempt to model more accurately conditions during aircraft poststall maneuvers and during helicopter high-speed forward flight. An airfoil was oscillated at pitch rates, $A = \dot{\alpha}c/2U$ between 0.001 and 0.020, Mach numbers between 0.2 and 0.4, and Reynolds numbers between 2–4 × 10⁶. Surface pressures were measured using 72 miniature transducers, and the locations of transition and separation were determined using 8 surface hot-film gages. The results demonstrate the influence of the leading-edge vorticity on the unsteady aerodynamic response during and after stall. The vortex is strengthened by increasing the pitch rate and is weakened by increasing the Mach number and by starting the motion close to the steady-state stall angle. A periodic pressure oscillation occurred after stall at high pitch angle and moderate Reynolds number; the oscillation frequency was close to that predicted for a von Kármán vortex street. A small supersonic zone near the leading edge at $M = 0.4$ was found to reduce significantly the peak suction pressures and the unsteady increments to the airloads. These results provide the first known data base of constant-pitch-rate aerodynamic information at realistic combinations of Reynolds and Mach numbers.

Nomenclature

A = pitch rate, $\dot{\alpha}c/2U$
c = airfoil chord, m
C_D = section pressure drag coefficient, D/Qc
C_L = section lift coefficient, L/Qc
C_M = section pitching-moment coefficient about $x/c = 0.25$, M/Qc^2
C_p = pressure coefficient, $(P - P_{static})/Q$
k = reduced frequency of sinusoidal motion, $\omega c/2U$
Q = freestream dynamic pressure, $P_{total} - P_{static}$, Pa
t = time from start of data acquisition, s
T = data-acquisition period, s
Re = Reynolds number, cU/ν
U = freestream velocity, m/s
x = distance from airfoil leading edge, m
α = geometric pitch angle, deg
ν = kinematic viscosity, m^2/s
ρ = air density, kg/m^3
τ = nondimensional time, t/T
ω = frequency of sinusoidal oscillation, $2\pi f$

Introduction

THE aerodynamic effect of rapidly pitching an airfoil beyond its steady-state stall angle has been studied by numerous investigators. An extensive period of experimentation occurred between the early 1960's and the mid-1970's. This work emphasized application to the retreating blade stall of a helicopter rotor that occurs in high-speed forward flight. Consequently, measurements were typically made of the unsteady sinusoidal pitching oscillations in the range of 0–20 deg, and at Mach and Reynolds numbers characterstic of the retreating blade of a helicopter ($M < 0.4$, $Re < 5 \times 10^6$). Representative efforts are reported in Refs. 1–4.

A more recent interest has developed in using the lift and drag augmentations that occur during dynamic stall to improve combat aircraft maneuverability.[5,6] Such maneuvers typically involve a rapid controlled pitching of the aircraft to a very high angle of attack at low to moderate Mach numbers. Several experiments have been performed to study constant-pitch-rate dynamic stall. The early work of Ham and Garelick[7] measured the surface pressure on a NACA 0012 airfoil that was pitched up to 20–30 deg at roughly constant nondimensional rates, $A = \dot{\alpha}c/2U$, between 0.005 and 0.02 and at the moderate Reynolds number of 3.4×10^5. Additional constant-pitch-rate experiments have been reported in Refs. 8–12. These studies have concentrated on obtaining airload and flow-visualization results for large-amplitude motions (up to $\alpha = 90$ deg) at high pitch rates (up to $A = 1.0$). However, this work was conducted at Mach numbers less than 0.1 and Reynolds numbers between 4×10^4 and 3×10^5, values substantially below those of a typical fighter wing during low-speed maneuvers ($10^6 < Re < 10^8$). Steady-state measurements for $Re < 5 \times 10^5$ indicate that stall frequently occurs when the laminar upper-surface flow separates near the leading edge.[13] This process leads to large steady-state stall hysteresis. A turbulent boundary-layer separation is more common at higher Reynolds number. It is possible that the unsteady stall characteristics also differ with Reynolds number.

The current experiment was designed to provide detailed aerodynamic information at a more representative scale. Earlier dynamic stall studies at the United Technologies Research Center (UTRC) used a tunnel-spanning wing system to oscillate an airfoil in a sinusoidal motion.[14,15] A new version of this apparatus has been built, incorporating a high-response hydraulic drive system capable of producing arbitrary airfoil pitching motions. The first use of this system was to measure surface pressures and flow conditions for a series of constant pitch rate ramps and sinusoidal oscillations at Mach numbers between 0.2 and 0.4, Reynolds numbers between 2 and 4×10^6, and pitch rates between $A = 0.001$ and 0.02.

Received July 24, 1987; revision received Jan. 5, 1988.

*Associate Research Engineer. Member AIAA.
†Supervisor, Aerodynamics Group. Associate Fellow AIAA.

Experiment

The model wing consists of a set of fiberglass panels mounted on a steel spar that spans the 8 ft (2.44 m) test section of the UTRC Large Subsonic Wind Tunnel (Fig. 1). A Sikorsky SSC-A09 airfoil with a 17.3 in. (43.9 cm) chord was used (Fig. 2). This is a 9% thick supercritical section designed for low drag at high subsonic Mach numbers. The pitch angle of the model is set by hydraulic actuators that are attached to each end of the spar and controlled using a dual-channel closed-loop system. A digital waveform synthesizer provides the sinusoidal or ramp input to the hydraulic controller and triggers the data-acquisition system. This allows 1024 samples of each data channel to be acquired at identical positions during each cycle of the wing motion.

The wing-mounted instrumentation consists of 72 miniature pressure transducers and 8 surface hot-film gages. The pressure transducers are mounted inside the fiberglass skin and connected to the surface by short pipettes. This technique provides a point measurement on a smooth surface contour and retains a frequency response that is flat within 5% out to at least 5 kHz. Each group of 8 pressure transducers is connected to an electronic power distribution and switching circuit located inside the model. An ensemble average based on 20 cycles of the motion is digitized, converted to pressure coefficient, and stored on magnetic tape.

The primary chordwise pressure transducers are located in arrays of 18 on each surface, 0.5 chord-lengths from the tunnel centerline, and 2.3 chord-lengths from the side wall. The transducers are arranged in a segmented Gaussian array from $x/c=0.005$ to 0.99 to minimize the integration error in computing the sectional airloads. The other 36 transducers are in arrays located 1.8 amd 1.4 chord-lengths from the wall and are primarily intended for use in future swept-wing and finite-tip experiments. During this experiment, the additional, arrays were used to verify the two-dimensionality of the flow. With the exception of an apparent irregularity in the formation of the leading-edge vortex at $x/c=0.010$ at the stations furthest from the centerline, the data show only a small amount of spanwise variation. The pressure transducers are calibrated by placing the instrumented section of the wing inside an environmental chamber and recording the output voltages over the full expected range of pressures and temperatures. The data system is then able to correct for any thermal changes in each transducer's sensitivity and offset voltage. This technique, in combination with the acquisition of frequent wind-off transducer zeros, allows both mean and unsteady pressures to be determined to within $\pm 1\%$ of the calibration range. The data reported here do not include any corrections for wind-tunnel wall effects. The hot-film gages are located in an array parallel to the primary pressure array. The gage closest to the leading edge is at $x/c=0.026$, and that closest to the trailing edge is at $x/c=0.880$. No calibration was performed since the hot films are intended to provide only qualitative information on the location of transition, separation, and reattachment. Additional information on the experimental apparatus is given in Ref. 16.

Unsteady data were acquired for 36 constant-pitch-rate ramps and 9 sinusoidal oscillations, as shown in Table 1. The maximum pitch rate of 360 deg/s occurred at $A=0.02$ and $M=0.2$, and the minimum of 18 deg/s at $A=0.001$. The maximum rate is lower than the maximum reached in many smaller-scale experiments,[8-12] but is larger than that for both the "typical" ($A=0.0010$) and "minimum time" ($A=0.0044$) maneuvers described in Ref. 5. The wing angle of attack was limited by the support system to a maximum of 30 deg, again less than the maximum obtained in the smaller-scale tests, but sufficient to include all of the primary stall-related events at the pitch rates used. The airfoil motion for a ramp consists of an initial delay of several seconds at the minimum angle, a constant rate increase to the maximum angle, another delay at the maximum angle, and a return to the initial condition. Data are acquired only during a portion T of this cycle. Time

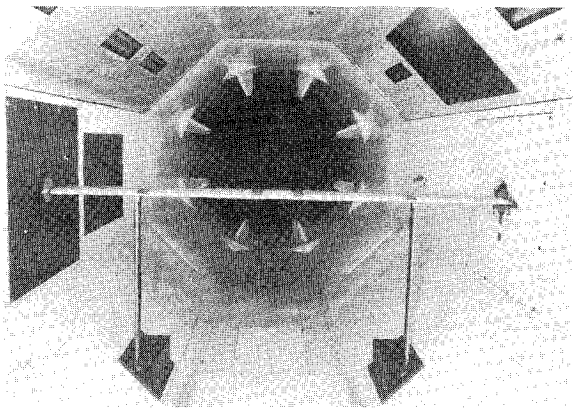

Fig. 1 Tunnel-spanning wing model in the 8 ft (2.4 m) test section of the UTRC wind tunnel.

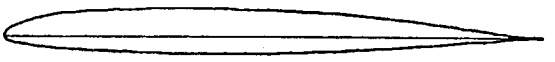

Fig. 2 SSC-A09 airfoil section.

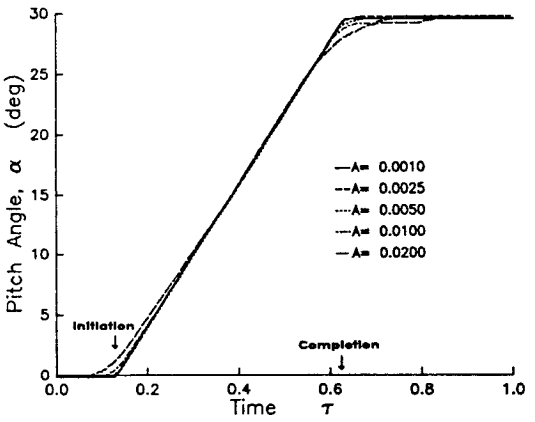

Fig. 3 Time histories of the pitch angle for 0–30 deg ramps at $M=0.2$.

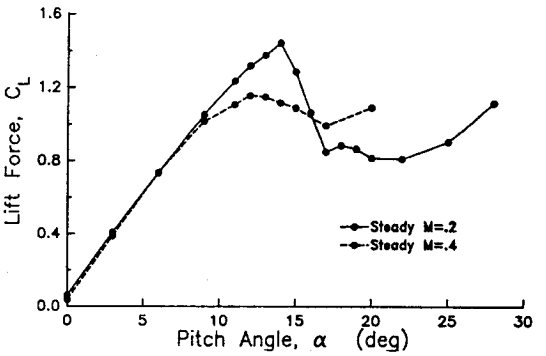

Fig. 4 Steady-state lift at $M=0.2$ and 0.4.

histories of the pitch angle during the data-acquisition period are shown in Fig. 3 for several 0–30 deg ramps at $M=0.2$. The ramp begins at a nondimensional time $\tau=t/T$ of 0.125 and ends at $\tau=0.625$. The pitch increase is quite linear with time and has sharp corners for $A<0.0050$. At higher pitch rates, the damping of the hydraulic system rounds the corners, but still maintains a nearly linear pitch rate near stall.

Steady-State Results

Steady pressure data were acquired at $M=0.2$ and 0.4. As shown in Fig. 4, the SSC-A09 airfoil has conventional stall

characteristics at these Mach numbers. At $M=0.2$, the maximum C_L of 1.4 is reached at $\alpha=14$ deg and followed by a rapid drop to a C_L of 0.9 at $\alpha=17$ deg. Increasing the Mach number to 0.4 reduces the maximum C_L to 1.2 and flattens the stall. The pressure distributions include a very strong leading-edge suction peak prior to stall. The maximum suction pressure occurs near $\alpha=13$ deg and reaches values of $C_p=-8.2$ at $M=0.2$ and $C_p=-5.2$ at $M=0.4$, as shown in Fig. 5. Since the sonic pressure coefficient at $M=0.4$ is -3.7, a small supersonic zone exists at the leading edge, terminated in a shock near $x/c=0.03$. The compressibility effects associated with this zone create the lift-curve differences seen in Fig. 4. Between $\alpha=15$ and 17 deg, the flow is separated over the rear of the airfoil at both Mach numbers, but maintains a pressure gradient near the leading edge. At higher angles of attack, the region of attached flow disappears at $M=0.2$ and is greatly reduced at $M=0.4$. These steady characteristics indicate that stall is caused by massive separation of a turbulent boundary layer, rather than by the bursting of a laminar leading-edge bubble.

Table 1 Test conditions studied

M	α Range, deg	Ramps, Pitch rate 0.0010	0.0025	0.0050	0.0100	0.200
0.2	0–10	x	x	x	x	
	0–20	x	x	x	x	
	0–30	x	x	x	x	x
	10–20	x	x	x	x	
	12–22	x		x	x	
	14–24				x	
	20–30	x	x			
	20–10	x			x	
	30–0	x		x		
0.3	0–20			x		
	0–30				x	
0.4	0–10	x		x		
	0–20	x	x	x	x	
	20–0				x	

Sinusoids

M	α, $\cos\omega t$	Reduced frequency, k 0.025	0.050	0.100
0.2	6–6	x		
	10–10	x	x	x
	20–20	x	x	x
0.3	9–8		x	
	12–8			x

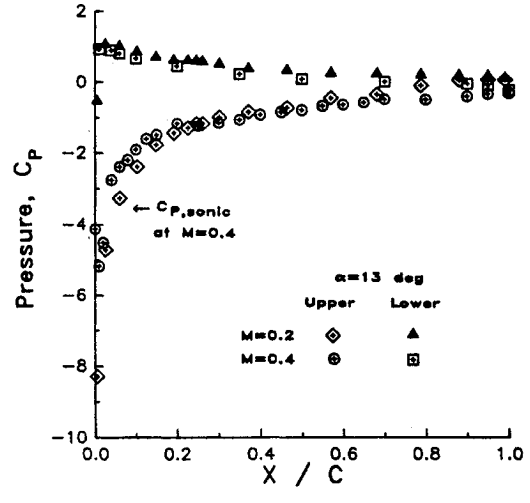

Fig. 5 Steady-state pressures at $\alpha=13$ deg for $M=0.2$ and 0.4.

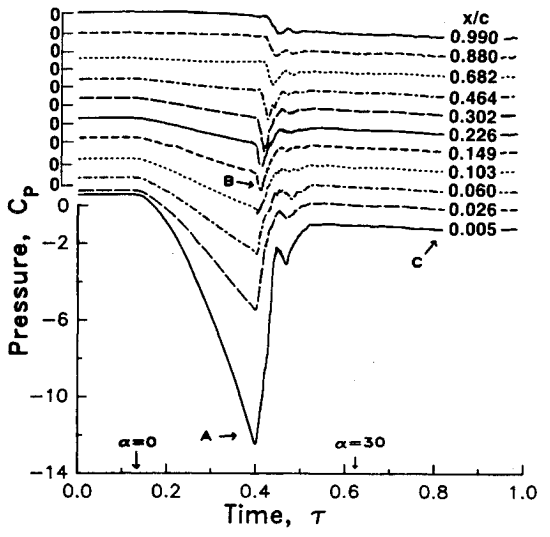

Fig. 6 Upper-surface pressure-coefficient time histories for a 0–30 deg ramp at $M=0.2$ and $A=0.005$.

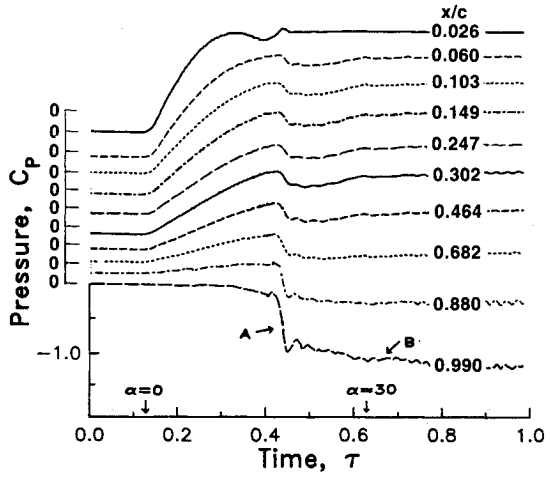

Fig. 7 Lower-surface pressure-coefficient time histories for a 0–30 deg ramp at $M=0.2$ and $A=0.005$.

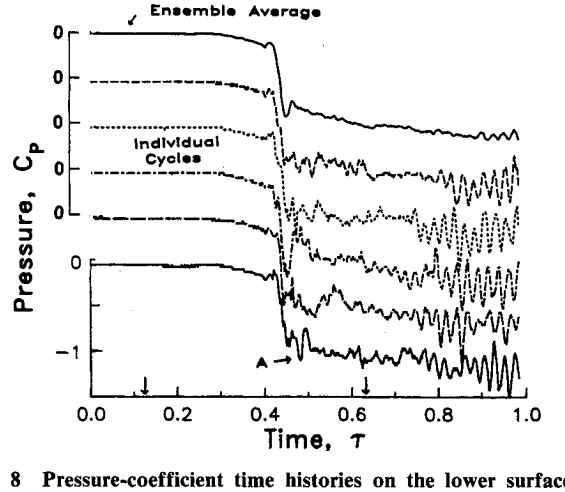

Fig. 8 Pressure-coefficient time histories on the lower surface at $x/c=0.99$; ensemble-averaged and individual cycle results for a 0–30 deg ramp at $M=0.2$ and $A=0.005$.

Results for an $A=0.005$, $M=0.2$ Ramp

The characteristics of constant-pitch-rate motion at $M=0.2$ will be discussed using the example of a 0–30 deg ramp at $A=0.0050$. The ensemble-averaged upper-surface pressure time histories for 11 of the 18 chordwise locations are shown in Fig. 6. The ordinate scale on the lower left refers absolutely to the curve for $x/c=0.005$. For clarity, each additional curve is offset vertically by $\Delta C_p=1.0$, and each curve is referenced to its own origin, as indicated by the upper left scale. The pressure responds smoothly to the imposed pitch angle until maximum suction is reached at $\tau=0.40$ ($\alpha=15.5$ deg). This is identified as letter A in Fig. 6. At this time, the peak suction pressure at $x/c=0.005$ is $C_p=-12.5$, which corresponds to a local Mach number of 0.84. The rapid local increase in pressure associated with passage of a vortex (B) is only observed for $x/c>0.1$, implying that the stall vortex forms ahead of this position and travels downstream after its release. This pressure disturbance propagates along the airfoil chord at at a speed of $0.16U$ and reaches the trailing edge at $\tau=0.45$. For $\tau>0.50$, the upper-surface separation is massive and the pressures vary little with either time or position along the chord (C). All of the stall-related events are completed well before the airfoil motion stops at $\tau=0.625$.

The lower surface does not separate and therefore has pressure time histories that are quite different, as shown in Fig. 7. There is vertical shift of the successive curves in this figure of $\Delta C_p=0.25$. The pressures near the leading edge are influenced by the motion of the stagnation point aft to $x/c=0.060$ at $\tau=0.40$, and then forward to $x/c=0.026$ following stall. Downstream of stagnation, the pressures generally respond smoothly to the changes in pitch. An exception is a rapid change when the upper surface separates at $\tau=0.40$ (A in Fig. 7). The largest change at this time occurs near the trailing edge, where the pressure is required to match that on the upper surface. A periodic oscillation in the ensemble-averaged pressures is also present at the rear of the lower surface (B). The oscillation frequency of 62 Hz is a very close to the 65 Hz frequency calculated for the von Kármán vortex street shed by a circular cylinder having a diameter D equal to the vertical projection of the airfoil chord, $c\sin\alpha$. As discussed in Ref. 17, a cylinder will generate a vortex street at a Strouhal number fD/U of 0.21 for Reynolds numbers less than 10^6 and at $fD/U=0.27$ for $Re>3\times10^6$. No regular vortex street is formed when the Reynolds number is between these limits. The Reynolds number of the cylinder equivalent to this airfoil at $M=0.2$ and $\alpha=30$ deg is 10^6, a value near the boundary where periodic oscillations should cease.

A larger poststall oscillation amplitude is found for individual records of the motion than for the ensemble average. The top time history in Fig. 8 represents the ensemble-averaged lower-surface pressure at $x/c=0.99$, whereas the lower five curves represent individual records. Each curve is offset vertically by $\Delta C_p=0.5$. The oscillations have the same frequency and a similar maximum amplitude during each record, but

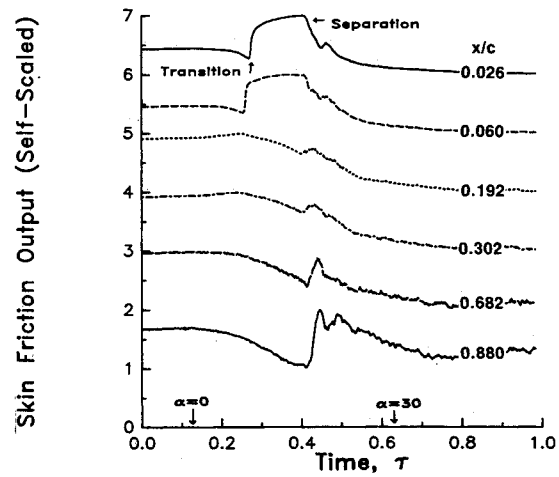

Fig. 10 Skin-friction gage time histories for a 0–30 deg ramp at $M=0.2$ and $A=0.005$.

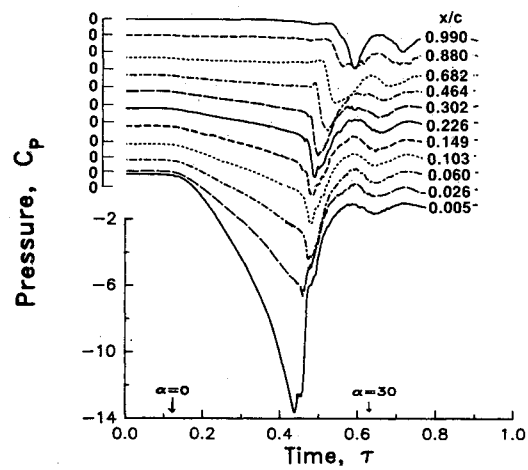

Fig. 11 Upper-surface pressure time histories for a 0–30 deg ramp at $M=0.2$ and $A=0.020$.

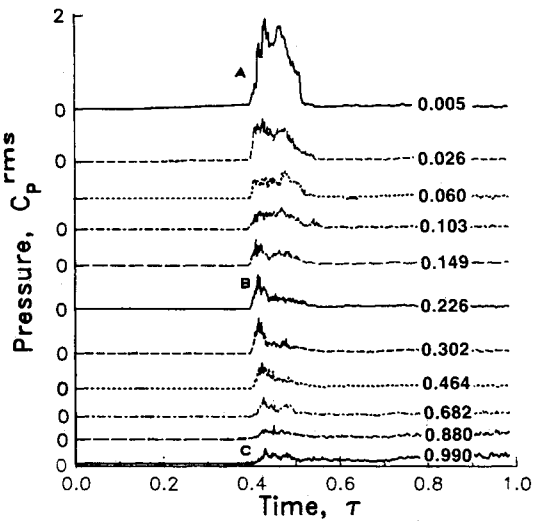

Fig. 9 Time histories of the root-mean-square upper-surface pressure coefficient for a 0–30 deg ramp at $M=0.2$ and $A=0.005$.

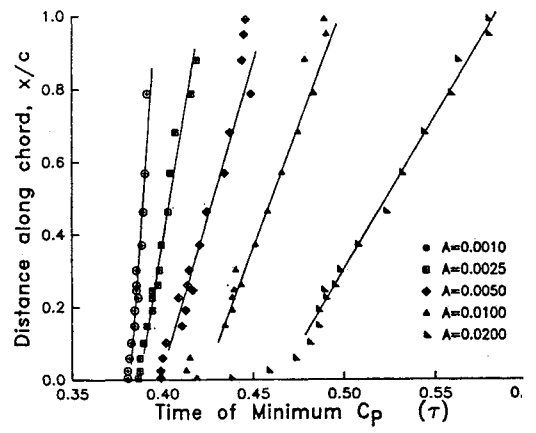

Fig. 12 Location of the stall vortex for 0–30 deg ramps at $M=0.2$, as determined by the times of minimum pressure.

they are not very well correlated in phase. The resulting cancellation greatly reduces the ensemble-averaged amplitude. A separate oscillation at a lower frequency is frequently present immediately following the passage of the stall vortex at $\tau = 0.45$ (A in Fig. 8). (Neither oscillation begins when the pitching motion starts or stops. The oscillations are not at the natural frequency of the support system. Therefore, they are unlikely to originate in the drive system.)

A quantitative measure of the degree of randomness is provided by the root-mean-square (rms) variation of the individual records about the ensemble average. Figure 9 shows time histories of the rms pressure coefficient on the upper surface. The curves are offset vertically and each begins at a value of approximately 0. The rms is greatest during separation ($0.4 < \tau < 0.5$) and near the leading edge (A). Aft of the stall vortex release point ($x/c = 0.1$), the rms has a peak that corresponds to the passing vortex (B). Near the trailing edge, this peak is preceded by a region of more gradual increase in the rms (C), implying that irregular pressure disturbances caused by stall reach the downstream stations ahead of the vortex. The rms at the rear of the airfoil also has an overall increase after stall caused by the nonsynchronous oscillations induced by the vortex street.

Hot-Film Gage Results

Further information on the surface flow conditions is provided by the hot-film gages. Ensemble-averaged time histories of the hot-film output at six stations are shown in Fig. 10. The data are self-scaled so that the difference between the maximum and minimum values is one unit. The boundary layer is initially laminar at $x/c = 0.026$ and 0.060 and is always turbulent for $x/c > 0.1$ (the gage at $x/c = 0.103$ was not functioning during this run, but indicated turbulent flow at similar conditions during other runs). The transition point, as indicated by a rapid rise in heat transfer, moves forward past $x/c = 0.060$ at $\tau = 0.241$ ($\alpha = 7.0$ deg) and past $x/c = 0.026$ at $\tau = 0.254$ ($\alpha = 7.7$ deg). Transition occurs ahead of $x/c = 0.026$ for the remainder of the cycle. (Appendix A describes a new method that has been developed to determine the transition point from the rms pressures. This technique may allow this information to be obtained much more easily in complex unsteady or three-dimensional flows, in particular when pressure transducers are the primary instrumentation.)

Ahead of the stall vortex release point ($x/c = 0.1$), the heat transfer drops when the boundary layer separates at $\tau = 0.40$. Downstream of the release point, the heat transfer drops slightly at separation but then rises rapidly as the high velocities induced by the stall vortex pass each gage. There is excellent agreement between the times of separation as measured by the hot-film gages and the adjacent pressure transducers.

Location of transition in unsteady flow at high Reynolds number is primarily influenced by changes in the pitch rate. The forward motion of the transition point is delayed by increasing the pitch rate. As indicated by the hot-film results of Ref. 16, transition passes the gages at a pitch angle about 2 deg higher at $A = 0.020$ than at $A = 0.001$. Doubling the freestream velocity to produce $M = 0.4$ and $Re = 4 \times 10^6$ causes minor changes in the motion of the transition point. At the same nondimensional pitch rate, transition moves forward at pitch angles only 0.2–0.3 deg lower than at $Re = 2 \times 10^6$ (Ref. 16).

Effect of Pitch Rate

Detailed pressure and hot-film data for five 0–30 deg ramps at $M = 0.2$ are presented in Ref. 16. Only the $A = 0.02$ upper-surface pressure results are presented here (Fig. 11). Qualitative similarity exists before stall; the primary differences occur during and after stall. The unsteady increments to the airloads are strongly influenced by the vorticity that is associated with the leading-edge suction peak before stall and forms the stall vortex afterward. The strength of the stall vortex may be estimated by measuring the change in C_p induced at $x/c = 0.302$. This increment increases from $\Delta C_p = 1.0$ at $A = 0.001$ to $\Delta C_p = 1.5$ at $A = 0.005$ and to $\Delta C_p = 2.5$ at $A = 0.020$. The speed with which the vortex travels downstream may be estimated using the times of minimum pressure at each transducer. Figure 12 shows these times at five pitch rates. The region of constant vortex speed generally begins near 0.10 and ends near $x/c = 0.80$ and 0.90. The speed in this region increases approximately linearly with pitch rate, from $0.13U$ at $A = 0.001$ to $0.33U$ at $A = 0.020$. Both the location of the constant-speed region and the variation with pitch rate are consistent with the results of Ref. 15 for a sinusoidally oscillating NACA 0012 airfoil at similar values of M and Re.

The poststall pressure oscillations noted earlier change character at pitch rates above $A = 0.010$. At all lower pitch rates, the persistent oscillations have frequencies between 59 and 62 Hz and do not occur with the same phase during each individual record. By $A = 0.020$, the oscillations have a frequency of 51 Hz and are synchronized with the imposed airfoil motion

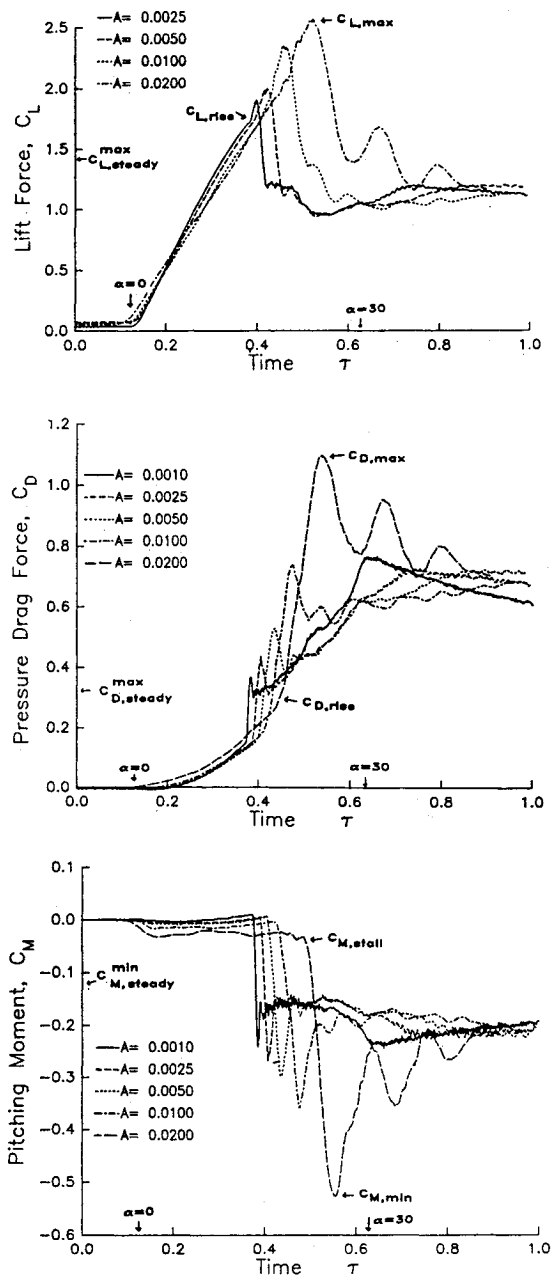

Fig. 13 Lift, moment, and drag time histories for 0–30 deg ramps at $M = 0.2$.

and with the stall vortex, producing the large pressure response indicated by A in Fig. 11. Large oscillations are also observed in the integrated force and pitching-moment results shown in Fig. 13. Previous studies of sinusoidal motions of several airfoil sections at $Re = 3\text{–}4 \times 10^6$ produced similar poststall oscillations for some, but not all, of the sections.[18] Jumper et al.[9] also observed large oscillations in the lift response during constant-rate ramps of a NACA 0015 airfoil at pitch rates similar to the current values but at smaller scale ($1.5 \times 10^5 < Re < 2.8 \times 10^5$ and $M < 0.05$). Other studies at apparently similar conditions[11,12] did not show such large oscillations. The differences among the results at lower Reynolds number may result from differences in airfoil shape or the wind-tunnel turbulence level and mounting technique. These have been shown to cause significant differences between steady-state results at low Reynolds numbers.[13] It is therefore not clear what, besides high pitch rate, is required to produce strong and synchronized poststall oscillations.

The integrated lift, pressure drag, and pitching moment (Fig. 13) show the anticipated qualitative trends with increasing pitch rate: 1) Before the stall vortex is formed, increasing the pitch rate decreases the lift slope, decreases the pitching moment, and increases the drag. The lift slope effect agrees with the results of Ref. 9 at lower Reynolds number. 2) There is a rapid buildup of lift (Fig. 13a) as the leading-edge vortex forms. The unsteady increment added to the quasisteady lift increases from $\Delta C_L = 0.4$ at $A = 0.001$ to $\Delta C_L = 1.1$ at $A = 0.020$. 3) The pressure drag (Fig. 13b) increases smoothly before stall, rises and falls rapidly as the stall vortex travels over the chord, and then increases slowly as the pitching of the airfoil rotates the aerodynamic force vector. 4) The pitching moment (Fig. 13c) in attached flow becomes more negative at higher pitch rate, following the prediction of thin airfoil theory (Appendix B). 5) The peak negative C_M after stall increases with pitch rate, from $C_M = -0.22$ at $A = 0.001$ to $C_M = -0.52$ at $A = 0.020$.

The sequence of the stall events as a function of pitch rate is shown in Fig. 14. The process begins when vorticity is concentrated near the leading edge and C_L and C_D start to rise. Moment stall occurs when the stall vortex is released. The maximum C_L occurs as the vortex travels downstream along the chord, and when the vortex approaches the trailing edge, the minimum C_M and maximum C_D are obtained. At these pitch rates, the angle when moment stall occurs increases approximately linearly with A, in agreement with earlier results for a sinusoid at similar peak pitch rates.[15] This linear dependence at low pitch rate does not agree with the square root of pitch-rate correlation postulated by Gormont.[19]

Results at Higher Mach Number

The influence of the leading-edge supersonic zone at $M = 0.4$ on the unsteady upper-surface pressures is illustrated in Fig. 15. The time histories for this 0–20 deg ramp at $A = 0.005$ are not shifted vertically: the same scale applies to all of the curves. At $x/c = 0.005$, the flow becomes supersonic at $\tau = 0.34$ ($\alpha = 7.6$ deg) and reaches a peak local Mach number of 1.3 at $\tau = 0.45$ ($\alpha = 10.6$ deg). The sharp rise and fall of the pressure at $x/c = 0.026$ (A in Fig. 15) are caused by the movement of the shock downstream past this station at $\tau = 0.40$ and back upstream at $\tau = 0.46$. A distinct stall vortex is released at $\tau = 0.46$ and $x/c = 0.060$, just downstream of the shock (B). Several of the vortex characteristics differ from those at $M = 0.2$: 1) the release point is at $x/c = 0.060$ instead of $x/c = 0.10$; 2) the vortex speed is approximately 10% less than the speed at $M = 0.2$; 3) the strength of the vortex is reduced by approximately 50%; and 4) the pressure signature of the vortex is not observed downstream of $x/c = 0.57$. In addition, no clearly defined oscillations are present after stall at $M = 0.4$. The Reynolds number of the equivalent bluff body is 1.4×10^6 for this case, above the maximum of 1×10 for a stable vortex street.[17] As was the case with the 0–30 deg ramp at $M = 0.2$, the principal stall-related events have been completed by the time motion stops at $\alpha = 20$ deg. Therefore, the results for the 0–20 deg ramp at $M = 0.4$ can be directly compared with the $M = 0.2$ results.

Figure 16 shows the time histories of C_L and C_M at $M = 0.4$ for 0–20 deg ramps at $A = 0.001$, 0.005, and 0.010. The vortex-induced peaks in C_L (Fig. 16a) are greatly reduced from the values at $M = 0.2$, especially at low pitch rate. For pitch rates below $A = 0.005$, the increment to C_L is less than 0.10 and the delay in the angle of maximum C_L is less than 1.5 deg. This suggests that compressibility prevents the development of the extremely strong suction peak seen at $M = 0.2$ and therefore reduces the strength of the stall vortex. The peak negative pitching moment (Fig. 16b) is also reduced. After stall, the absence of strong vortex shedding at the trailing edge allows C_L and C_M to approach relatively constant values that are approximately the same at all pitch rates studied.

Effect of Starting and Ending Angle

Changing the pitch angle at which the airfoil motion begins and ends may have a significant effect on both the stall and poststall characteristics. The largest changes occur if the combination of pitch rate and final pitch angle is such that the stall vortex has not reached the trailing edge when the motion ends.

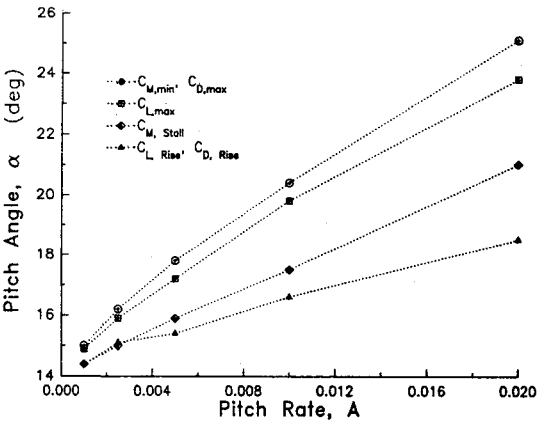

Fig. 14 Sequence of stall events as a function of pitch rate for 0–30 deg ramps at $M = 0.2$.

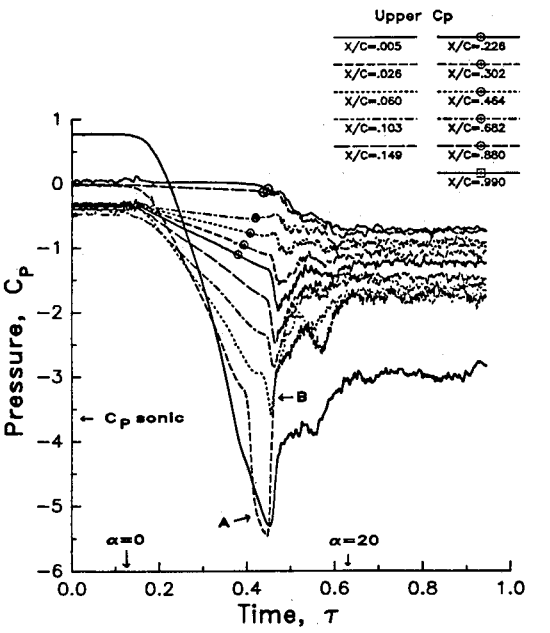

Fig. 15 Upper-surface pressure time histories for a 0–20 deg ramp at $A = 0.005$ and $M = 0.4$.

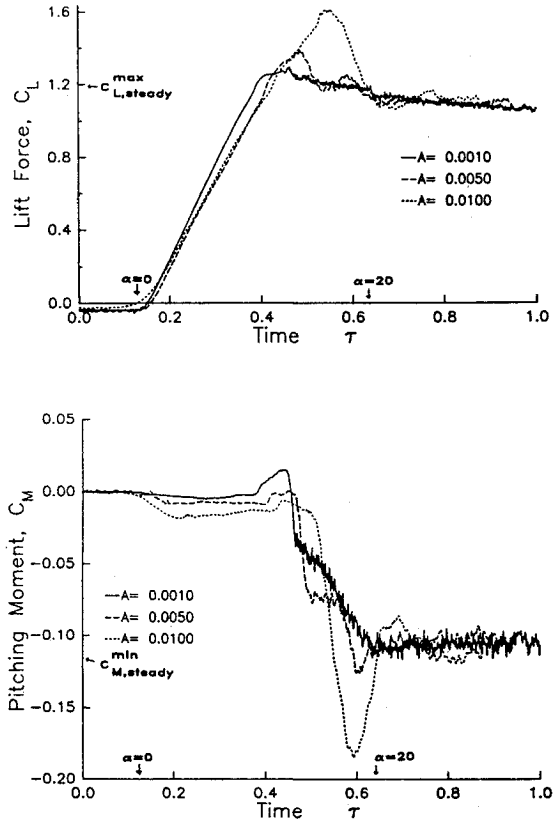

Fig. 16 Lift and moment time histories for 0–20 deg ramps at $M=0.4$.

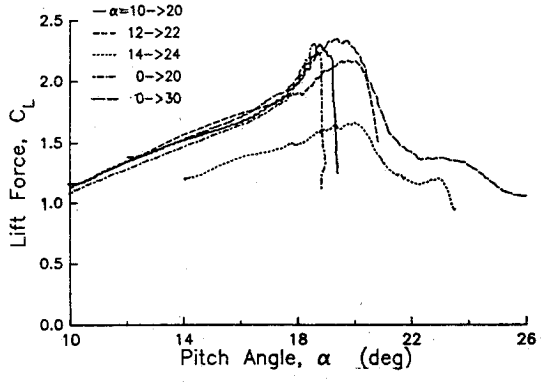

Fig. 17 Effect of pitch-angle range on unsteady lift for ramps at $A=0.01$ and $M=0.2$.

In such a case, the peak airloads are reduced, and a distinct stopping vortex is released near the leading edge. Figure 17 illustrates the effect of pitch range on lift for constant-pitch-rate ramps at $A=0.010$ and $M=0.2$. The premature termination of the stall process when the motion stops causes a rapid drop in C_L when the final angle is 20 or 22 deg. As shown by the times of minimum pressure for the 10–20 deg ramp in Fig. 18, the stall vortex appears to pause for $\Delta\tau=0.034$ and then resumes traveling downstream. The propagation speed is the same ($0.28U$) both before and after the pause and is also the same for all three pitch ranges at $A=0.010$. The pressure time histories for these cases[16] show the signature of the stopping vortex only near the leading edge, implying that this vortex merges with the stall vortex during the pause. Flow visualization would be useful in verifying this explanation.

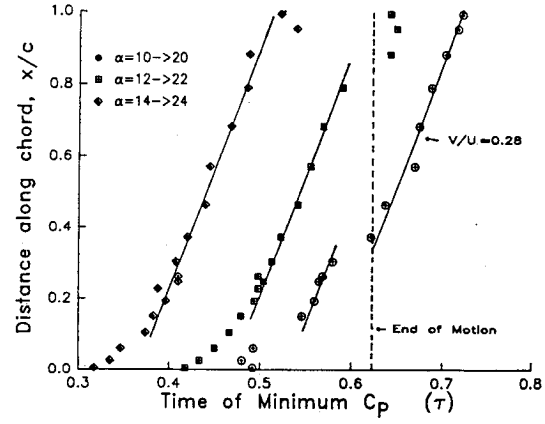

Fig. 18 Effect of pitch-angle range on the stall vortex propagation at $A=0.01$ and $M=0.2$.

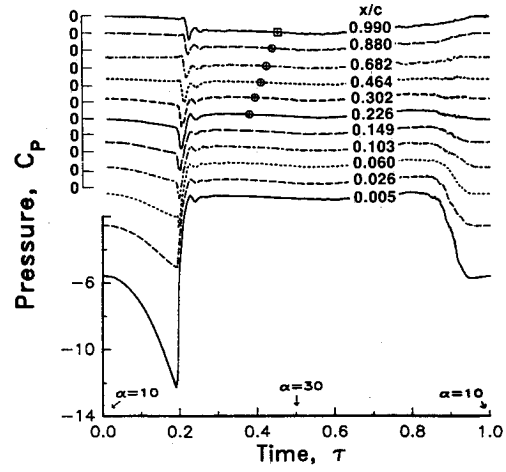

Fig. 19 Upper-surface pressure time histories for sinusoidal motion, $\alpha=20-10\cos\omega t$, at $k=0.025$ and $M=0.2$.

Figure 17 also shows how the initial angle of the motion affects the lift. For initial angles below the steady-state stall angle, the differences are small, but if the inital steady flow is already partially stalled, the maximum lift is significantly reduced. This occurs for the 14–24 deg ramp, where the maximum C_L is only 1.6, much less than the value of $C_L=2.3$ for the base (0–30 deg) case. The stall vortex strength, as measured by the change in pressure at $x/c=0.30$, is also reduced (by 30%).

Results for Sinusoidal Oscillations

Sinusoidal motion differs from ramp motion in two important respects: In a sinusoid, the airfoil does not start from a steady-state condition and the pitch rate is constantly changing. Nonetheless, there are many qualitative similarities between the responses to the two motions. Upper-surface pressure time histories for $\alpha=20-10\cos\omega t$ at $M=0.2$ and $k=0.025$ are shown in Fig. 19. The motion begins at $\tau=0.0$, reaches maximum pitch angle at $\tau=0.50$, and returns to the minimum value at $\tau=1.0$. Each time history in the illustration is offset vertically by $\Delta C_p=1.0$. The characteristics are similar to the constant-pitch-rate results at $A=0.005$ (Fig. 6).This is reasonable because the instantaneous pitch rate at stall is similar, $A=0.0042$. The stall vortex is released somewhat further upstream during the sinusoid ($x/c=0.06$ instead of 0.10), it is somewhat weaker ($\Delta C_p=1.3$ instead of 1.6), and propagates more rapidly ($0.25U$ instead of $0.16U$). The poststall

pressures for the sinusoid show a uniformity in space and time that is similar to the massive stall observed at constant pitch rate.

Conclusions

The primary results of this experimental investigation of dynamic stall at large Reynolds number and moderate Mach number include the following:

1) For constant-pitch-rate ramps, the unsteady aerodynamic response near stall is strongly dependent on the characteristics of the leading-edge vorticity. A stall vortex is released near $x/c=0.10$ during stall and propagates downstream at a constant velocity. The propagation speed, vortex strength, and unsteady increments to C_L, C_M, C_D all increase with pitch rate.

2) A periodic oscillation of the surface pressures occurs at high angle of attack when the equivalent bluff-body Reynolds number $Uc\ \sin\alpha/\nu$ is less than 10^6. At pitch rates above $A=0.01$, the oscillation synchronizes with the motion of the airfoil and increases in amplitude.

3) The location of boundary-layer transition to turbulence moves forward along the airfoil chord as the pitch angle increases. This shift is delayed at higher pitch rate, but is only slightly advanced by doubling the Reynolds number to 4×10^6.

4) A supersonic zone is formed near the leading edge at $M=0.4$. This zone reduces the peak suction pressures, unsteady airloads, and strength of the stall vortex.

5) Stopping the airfoil pitching motion before the stall vortex has passed the trailing edge generates a stopping vortex near the airfoil leading edge. This vortex combines with the stall vortex and, after a pause, it propagates downstream at a speed equal to that of the original stall vortex.

6) Starting the airfoil pitching motion at an angle above that at which the stall vortex would have begun to form weakens the vortex and reduces the unsteady increments to the airloads.

7) Results for sinusoidal oscillations are qualitatively similar to the results for ramp motions having the same values of M, Re, and A at stall, but contain quantitative differences in the stall vortex strength and propagation speed.

Appendix A: Determination of Transition from the rms Pressure

Accurate determination of the point of boundary-layer transition is critical to many numerical computations. Surface heat-transfer gages are usually required to determine the unsteady motion of the transition point. These gages are frequently cumbersome to install and each requires an individual active anemometer circuit. Examination of the time-history results for this experiment has shown that it may be possible to locate the transition using unsteady pressure transducers to measure the increased rms pressures caused by a turbulent boundary layer. An example of the correlation between the hot-film and pressure transducer results is shown in Fig. A1.

All results are at $x/c=0.026$ for a 0–30 deg ramp at $A=0.050$ and $M=0.20$. The increase in pressure rms corresponds to the increase in ensemble-averaged heat transfer and the spike in rms heat transfer. No change at transition is apparent in the ensemble-averaged pressure. If these promising early results are confirmed by additional correlations, this method may make it much easier to locate transition in complex three-dimensional and unsteady flows.

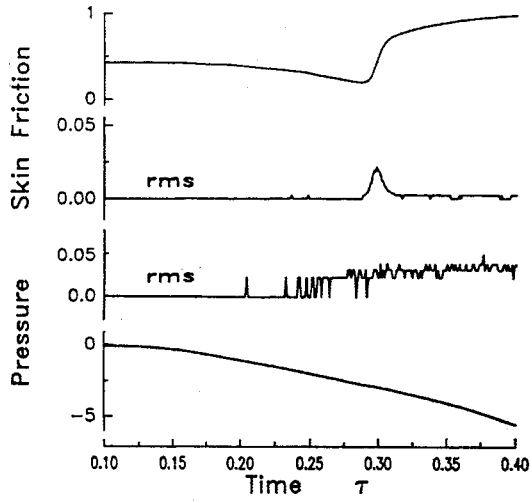

Fig. A1 Determination of transition from rms pressure time histories for a 0–30 deg ramp at $A=0.02$ and $M=0.2$.

Appendix B: Pitching-Moment Offset in Attached Flow

In attached flow at moderate angles of attack, the section force and moment coefficients may often be accurately estimated using unsteady thin airfoil theory. For a constant-rate pitching motion about the quarter-chord of the section, the expression for the pitching moment (Eqs. 4–171 in Ref. 20) is reduced to a single term

$$M=-(\tfrac{1}{8})\pi\rho c^3 U\dot{\alpha}$$

or, in terms of the nondimesional parameters,

$$C_M=-(\tfrac{1}{2})\pi A$$

The results for the 0–30 deg ramps at $M=0.2$ presented in Fig. 13c are summarized in Table B1.

Table B1 Test conditions

A	C_M theory	C_M expt.
0.0010	0.0016	0.0020
0.0025	0.0040	0.0045
0.0050	0.0079	0.0080
0.0100	0.0157	0.0160
0.0200	0.0314	0.0300

Acknowledgment

This work was supported by the U. S. Air Force Office of Scientific Research under Contract F49620-84-C-0082, initiated by Dr. M. S. Francis and monitored by Dr. J. D. Wilson.

References

[1]Liiva, J. and Davenport, F. J., "Dynamic Stall of Airfoil Sections for High-Speed Rotors," *Journal of the American Helicopter Society,* Vol. 14, April 1969, pp. 26–33.

[2]Carta, F. O. and Niebanck, C. F., "Prediction of Rotor Instability at High Forward Flight Speeds, Volume III. Stall Flutter," U. S. Army Aviation Material Labs, Fort Eustis, VA, USAAVLABS Tech. Rept. 68-18C, Feb. 1969.

[3]McCroskey, W. J., McAlister, K. W., and Carr, L. W., "Dynamic Stall Experiments on Oscillating Airfoils," *AIAA Journal,* Vol. 14, Jan. 1976, pp. 57–63.

[4]Dadone, L. U., "Two-Dimensional Wind Tunnel Test of an Oscillating Rotor Airfoil," NASA CR-2914, Dec. 1977.

[5]Herbst, W. B., "Supermaneuverability," *Proceedings of the Air Force Office of Scientific Research/Frank J. Seiler Research Laboratory-Univ. of Colorado Workshop on Unsteady Separated Flows,* U. S. Air Force Academy, Colorado Springs, CO, Aug. 1983.

[6]Lang, J. D., "Unsteady Aerodynamics and Dynamic Aircraft Maneuverability," *Unsteady Aerodynamics*—Fundamentals and Application to Aircraft Dynamics, Advisory Group for Aerospace Research and Development, Nov. 1985.

[7]Ham, N. D. and Garelick, M. S., "Dynamic Stall Considerations in Helicopter Rotors," *Journal of the American Helicopter Society,* Vol. 13, April 1968, pp. 49–55.

[8]Daley, D. C. and Jumper, E. J., "Experimental Investigation of Dynamic Stall for a Pitching Airfoil," *Journal of Aircraft,* Vol. 21, Oct. 1984, pp. 831–832.

[9]Jumper, E. J., Schreck, S. J., and Dimmick, R. L., "Lift-Curve Characteristics for an Airfoil Pitching at Constant Rate," AIAA Paper 86-0117, Jan. 1986.

[10]Walker, J. M., Helin, H. E., and Chou, D. C., "Unsteady Surface Pressure Measurements on a Pitching Airfoil," AIAA Paper 85-0532, March 1985.

[11]Francis, M. S., Keese, J E., "Airfoil Dynamic Stall Performance with Large Amplitude Motions," *AIAA Journal,* Vol. 23, Nov. 1985, pp. 1653–1659.

[12]Strickland, J. H. and Graham, G. M., "Force Coefficients for a NACA-0015 Airfoil Undergoing Constant Pitch Rate Motions," *AIAA Journal,* Vol. 25, April 1987, pp. 622–624.

[13]Marchman, J. F., "Aerodynamic Testing at Low Reynolds Numbers," *Journal of Aircraft,* Vol. 24, Feb. 1987, pp. 107–114.

[14]St. Hilaire, A. O., Carta, F. O., Fink, M. R., and Jepson, W. D., "The Influence of Sweep on the Aerodynamic Loading of an Oscillating NACA 0012 Airfoil. Volume 1—Technical Report," NASA CR-3092, May 1979.

[15]St. Hilaire, A. O. and Carta, F. O., "Analysis of Unswept and Swept Wing Chordwise Pressure Data from an Oscillating NACA 0012 Airfoil Experiment. Volume 1—Technical Report," NASA CR-3567, March 1983.

[16]Lorber, P. F. and Carta, F. O., "Unsteady Stall Penetration Experiments at High Reynolds Number," United Technologies Research Center Rept. R87-956939-3, April 1987 (also AFOSR-TR-87-1202).

[17]Schlichting, H., *Boundary Layer Theory,* McGraw-Hill, New York, 1979, pp. 31–32.

[18]McAlister, K. W., Pucci, S. L., McCroskey, W. J., and Carr, L. W., "An Experimental Study of Dynamic Stall of Advanced Airfoil Sections, Volume II—Pressure and Force Data," NASA TM-84245, Sept. 1982.

[19]Gormont, R. E., "A Mathematical Model of Unsteady Aerodynamics and Radial Flow for Application to Helicopter Rotors," U. S. Army Air Mobility Research and Development Laboratory Tech. Rept., 72–67, May 1973.

[20]Bisplinghoff, R. L. and Ashley, H., *Principles of Aeroelasticity,* Wiley, New York, 1962, p. 120.